PERGAMON

International Journal of Solids and Structures 37 (2000) 3919–3934

INTERNATIONAL JOURNAL OF SOLIDS and STRUCTURES

www.elsevier.com/locate/ijsolstr

Experimental verification of buckling-mode interaction in intermediate-length composite columns

Ever J. Barbero*, Edgar K. Dede, Shannon Jones

315 Engineering Science Building, West Virginia University, Morgantown, WV 26506-6106, USA

Received 10 October 1998

Abstract

Column buckling is a major design concern for pultruded composite columns. Interaction between the local (flange) and global (Euler) buckling modes occurs in intermediate length thin-walled columns with near coincident buckling loads. The interaction of more than one buckling mode induce an unstable tertiary post-buckling path, causing imperfection sensitivity and premature failure. In this work, the existence of buckling-mode interaction is experimentally verified for intermediate length pultruded wide-flange columns subjected to uniaxial compression. Characterization of the interaction mode is done using both conventional testing techniques and the shadow moiré optical technique, allowing for non-contact, full field measurement of the buckling modes. © 2000 Elsevier Science Ltd. All rights reserved.

Keywords: Pultrusion; FRP; Buckling; Mode interaction; Experimental

1. Introduction

When a polymer resin is reinforced with fibrous material, it is called a composite material or a Fiber Reinforced Plastic (FRP). Composite structural shapes are produced by pultrusion, with the geometry and material properties of the cross-section being fixed by the manufacturer. A broad selection of such shapes is offered (PULTEX 1999; Strongwell, 1994). They are used because of their high strength to weight ratio, resistance to environmental deterioration, and lack of interference with electromagnetic radiation. Since composite columns are thin-walled, buckling is a major consideration in design. Two types of column failure (buckling) are well known: local (flange) and global (Euler) column buckling.

* Corresponding author. Fax: +1-304-293-6689.
E-mail address: ebarbero@wvu.edu (E.J. Barbero).

0020-7683/00/$ - see front matter © 2000 Elsevier Science Ltd. All rights reserved.
PII: S0020-7683(99)00172-9

The interaction between these two modes for intermediate length columns is the object of this investigation.

Local buckling occurs in short columns that are long enough not to fail due to crushing; that is when the compression strength of the material is not reached (Barbero, 1998a). For pultruded wide-flange (WF) sections (Fig. 1), the column will compress axially until flanges develop wave like deformations along the length. The flange deformations can be large, often greater than the thickness of the flanges. Therefore the local buckling load can be used as a failure criteria for a short column. The short column buckling load P_L can be determined from a short column test (Tomblin and Barbero, 1994) or predicted using analytical or numerical techniques (Banks and Rhodes, 1983, etc.). Its value is independent of the length of the column as long as the column is short (see Fig. 2) and wave amplitude modulation is not a factor.

The Euler (global) mode occurs in slender columns and involves a sudden lateral deflection without deformation of the cross-section. The Euler buckling equation

$$P_E = \frac{(EI)}{(kL/\pi)^2} \tag{1}$$

accurately predicts the critical buckling load for slender columns in terms of the bending stiffness (EI), the column length L, and the end-restraint coefficient k. Therefore, the Euler buckling load can be used as a failure criteria for a slender column. The reduction of buckling load due to shear deformation can be accounted for by dividing the result of Eq. (1) by $1+P_E/(GA)$, where (GA) is the shear stiffness of the section (Gaylord and Gaylord, 1972). In addition to being a small effect, the shear stiffness (GA) is not reported in product literature and it is difficult to measure accurately. It is customary in steel design to predict (GA) as the product of the material shear modulus times the area of the web, when bending occurs about the strong axis. However, for composite WF shapes bending about the weak axis, (GA) is not predicted accurately in this way (Barbero, 1998b, Chapter 8).

When the length of the column is such that the predicted local and Euler loads are close, the experimental failure load may be lower than both predictions, depending on the imperfections, as shown in this investigation. Based only on observed failure loads, Barbero and Tomblin (1994) proposed that the reduction is due to buckling-mode interaction. Stability theory (Bazant and Cedolin, 1991; Kasagi and Sridharan, 1995; Kabir and Sherbourne, 1998) predicts that there is a combination of the local and Euler modes at intermediate (interaction) lengths, resulting in lower buckling loads when compared to the individual contributing modes (local and Euler). An analysis of the perfect system (Godoy et al., 1995) reveals two bifurcations on the fundamental path corresponding to the isolated local and Euler

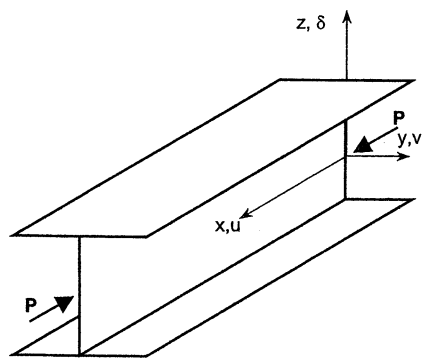

Fig. 1. Sample geometry and coordinate system.

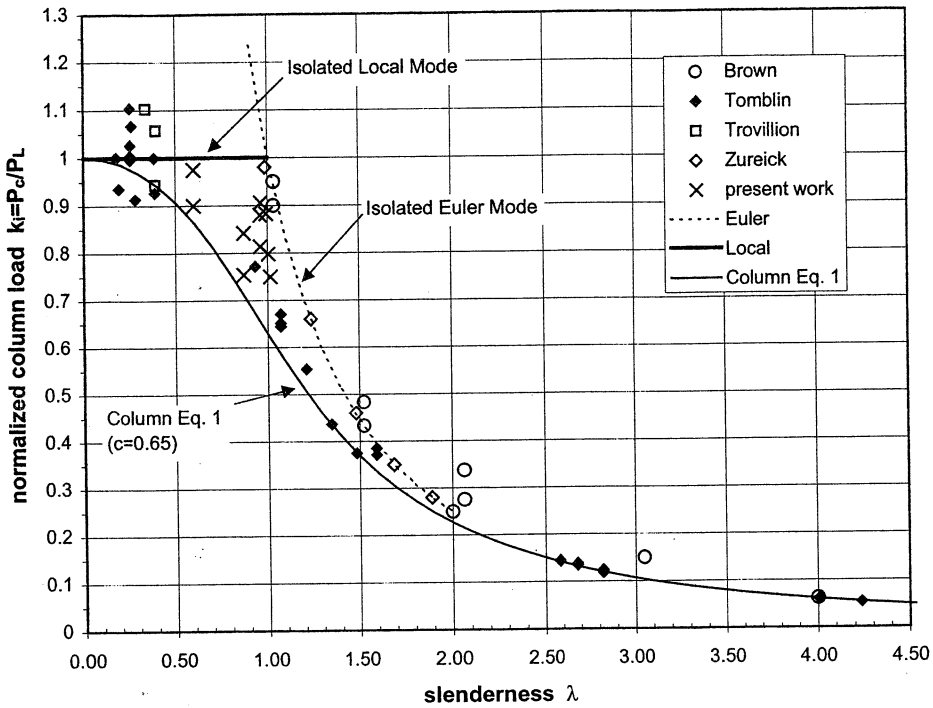

Fig. 2. Failure loads of columns subjected to axial load.

modes (Fig. 3). When these two bifurcation loads are close or coincident, a new bifurcation appears along the post-buckling path and a third path emerges from it. The buckling mode on this path is the interacting mode. Both the Euler and local path are stable but the third path may be unstable. If the path is unstable, the column is imperfection sensitive and the failure catastrophic. The magnitude of the

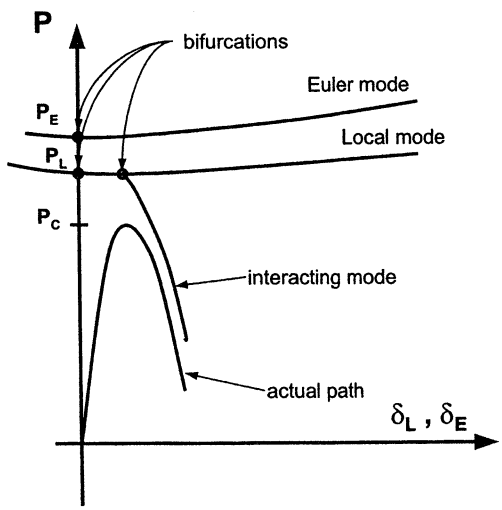

Fig. 3. Schematic behavior of the perfect and the actual (imperfect) systems during buckling mode interaction.

critical load P_C thus depends on the amount of imperfection present in each column. An empirical equation was then proposed (Barbero and Tomblin, 1994) to model the data from the literature (Brown et al., 1998; Zureick and Scott, 1997) which is shown in Fig. 2. According to the empirical equation, the column buckling load is predicted as

$$P_c = k_i P_L \tag{2}$$

where P_L is the short-column load, and the resistance factor k_i due to mode-interaction is

$$k_i = k_\lambda - \sqrt{k_\lambda^2 - 1/(c\lambda^2)} \tag{3}$$

where $k_\lambda = (1 + 1/\lambda^2)/2c$ is a coefficient introduced for convenience, "c" is the empirical interaction constant adjusted to fit the data and λ is the composite slenderness defined as

$$\lambda = \frac{kL}{\pi}\sqrt{\frac{P_L}{(EI)}} \tag{4}$$

where k is the end-restraint coefficient. The bending stiffness (EI) can be measured from a bending test (Bank, 1989) or back calculated from a slender-column test using Eq. (1).

Buckling mode interaction on Mylar shells was investigated experimentally by Foster (1981). A wealth of experimental data is available for plates but these show non-interacting stable postbuckling paths (Arbocz et al., 1985; Esslinger and Geier, 1975). Guidelines for testing metallic columns are provided by Galambos (1988) but these mostly involve interaction of a buckling mode with yield of the material. The scope of this study is to verify and quantify experimentally the existence of buckling-mode interaction in pultruded composite columns and to characterize the overall buckling behavior. Buckling-mode interaction is investigated using conventional test procedures (Barbero and Tomblin, 1994) coupled with the shadow moiré technique (Schwarz, 1988), capable of measuring full field, out-of-plane displacements. The contributions of the local and Euler modes to the overall buckling behavior of intermediate columns is readily observed, because the two conventional buckling modes (local and Euler) as well as the emerging interactive mode are characterized by distinct and measurable physical deformations.

2. Experimental setup

2.1. Buckling frame

The buckling-mode interaction tests were performed on a horizontal buckling frame (Fig. 4) about the weak axis of the specimens. All specimens were pultruded WF-columns provided by Creative Pultrusions Inc. (Table 1). The specimens were prepared using a band saw to cut the ends squarely with respect to the flange surface. It is critical to have the column ends cut flat and perpendicular to the column's axis,

Table 1
Properties for the structural shapes used

Type	Denomination	Flange thickness (mm)	(EI) (kN.m^2)	P_L (kN)	F_{xc} flange (MPa)	F_{xc} web (MPa)
A	6 × 6 × 1/4	6.35	89.6	170	283	290
B	8 × 8 × 3/8	9.53	380.0	370	320	221

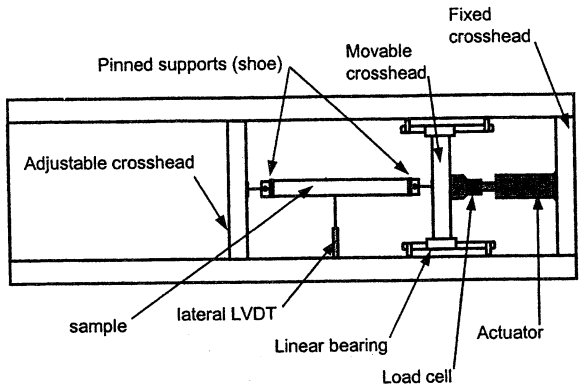

Fig. 4. Buckling frame.

mainly with respect to the strong axis to prevent premature localized failure. This may occur because the pin-and-needle bearings provide only one degree of rotational freedom around the weak axis of the column.

The columns were mounted in the frame in such a manner as to have one of the flange surfaces facing upwards, so that gravity acts on the strong axis, which is not tested. Therefore, there is no contribution to the Euler buckling mode due to gravity. The adjustable crosshead of the buckling frame (Fig. 4) adjusts in 305-mm increments, allowing for the testing of columns ranging in length from 1.2 to 6 m. Mounted to the inside of both the adjustable and the movable crosshead were two shoes with pin-and-needle bearings, which provide the pinned–pinned end conditions for the test.

A MTS 500 kN hydraulic actuator with a ±152-mm stroke is mounted between the fixed and movable crosshead. The actuator is equipped with an internal (stroke) LVDT used to measure the stroke position of the actuator. The load was measured using a load cell mounted on the actuator in the line of loading. In order to measure the lateral column movement due to Euler buckling, a ±127 mm PR750-5000 LVDT (lateral) was mounted to the side of the buckling frame and secured to the web of the sample using double sided tape.

The two displacement measurements (stroke and lateral) were conditioned using two MTS 458.14 conditioners, while the load was conditioned using one MTS 458.12 conditioner housed in a MTS 458.10 Microconsole. The conditioned data was then passed to the data acquisition software using a Metrabyte DAS 16 data acquisition card. The data was recorded and displayed using Labtech Notebook Pro ver. 8.0 (1994), installed on a 486/33 PC. The tests were performed using stroke–displacement control using a MTS 418.91 Microprofiler.

2.2. Shadow moiré

The shadow moiré optical technique (Schwarz, 1988) was used to measure out-of-plane displacements of the top flange. Since this is a non-contact technique, the development of the buckling mode is unaffected by the instrumentation. The full-field deformations are recorded in real time using a video acquisition system.

Creating the fringe field is accomplished by shining a light source at an angle α through a grating of desired frequency, producing a shadow or virtual grating on the surface of the specimen. When the physical and shadow gratings are parallel there are no fringes. Once the specimen experiences out-of-plane deformations, the shadow grating interferes with the physical grating, creating fringes when

viewed normal to the original grating. The amount of out-of-plane deformation that a specimen experience can be related by the number of fringes N_f, the pitch p of the grating, and the angle α between the light source and the normal to the grating

$$w = \frac{pN_F}{\tan \alpha} \tag{5}$$

with a resolution equal to the pitch of the grating. An angle $\alpha = 45°$ was used in this investigation. A grating with frequency 2.56 line/mm was used (ByChrome, 1995) to create a viewing area of 1300 × 250 mm. A viewing area wider than the sample is necessary because the column also deforms laterally. The three gratings were mounted on plate glass using silicone spray, which minimized air bubbles between the grating and the glass without evaporating and deteriorating the grating. The mounted glass was then suspended approximately 12.7–25.4 mm above the top flange surface of the specimen. The top flange surface was painted with flat white spray paint in order to enhance contrast. Choosing the top flange surface was a matter of visually inspecting both flange surfaces and picking the surface with the least amount of initial imperfections. The mounting frame used to suspend the grating enables free lateral adjustments from edge to edge of the frame and independent vertical adjustments at the four corners in order to zero the initial fringe field. Due to the initial imperfections of the columns and the high resolution of the technique, it was impossible to completely zero the initial field. Instead, the initial fringe pattern gives a contour plot of the initial imperfect shape of the flange.

2.3. Video acquisition

Tomblin and Barbero (1994) measured and manually recorded flange deformations for locally buckled columns using four dial gauges positioned along a column's length. In this project, a full-field optical recording method was developed to capture flange deformation at every point, in real-time. Video acquisition was used to record simultaneously the moiré image and the digital values of stroke, load, and lateral displacements.

A high resolution CCIR camera (COHU 4990) fitted with a 12 mm lens (f1.2-16), was used to view the test sample. A medium resolution camera (COHU 4913) fitted with a 6 to 1 lens was used to view the data acquisition display from the data acquisition computer (DAC). The video signal from the two cameras is fed to the video acquisition computer (VAC) via a serial connector on a MX-2MB frame grabber card. This connection keeps the two video-signals separate even though both must share the same input port. The video images were then compiled into one image using a program in Optimas (1993). The video output was sent to a SVHS VCR, which recorded the composite image. This composite image can later be captured, frame by frame, from the SVHS VCR using the Optimas video

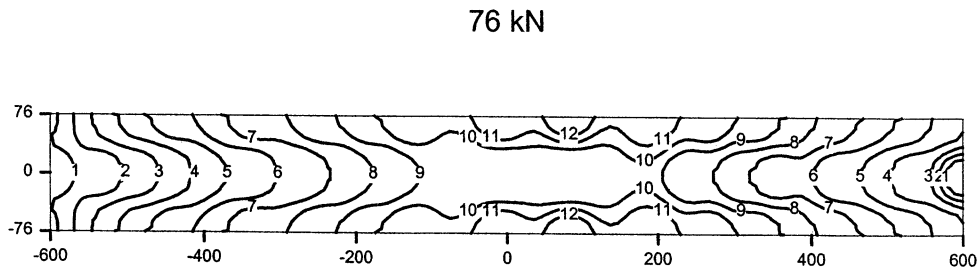

Fig. 5. Contour plot of flange deformations (fringe number) for sample 6 at $P/P_L = 0.447$.

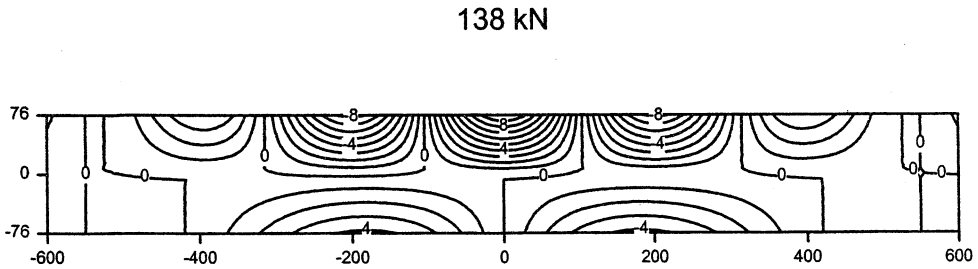

Fig. 6. Contour plot of flange deformations (fringe number) for sample 6 at $P/P_L = 0.812$.

acquisition software. The image is then digitized, the initial fringe readings are subtracted, and the result is shown as a contour plot (Figs. 5 and 6).

In order to view the desired 1300-mm test section, the high-resolution camera was suspended 2.9-m above the test specimen. The camera frame allows for lateral adjustments and vertical adjustments to center the camera above the specimen and obtain the desired field of view. Besides supporting the camera, the frame also provided a means of draping lengths of cloth in order to keep as much ambient light as possible from reaching the test sample, as this would degrade the contrast. Camera focus and aperture adjustments were needed to occur at the onset of each test. For safety and convenience, two geared, reversible DC motors were mounted next to the camera lens; one for the aperture, the other for focus. The motors were controlled using two, three position spring switches on a control box that allowed for remote operation, approximately 12 m from the test.

3. Experimental procedure and observations

Twelve specimens were prepared from the available WF-columns to various lengths, shown in Table 2. Each specimen was mounted into the grips and snuggled into place by moving the actuator until a slight load was read. The grating was then suspended above the specimen using the mounting fixture. The

Table 2
Comparison of experimental failure load P_C with three Southwell predictions of critical loads, normalized with the short-column load

Sample (type)	λ	P_C/P_L	P_V/P_L	$P_{(\delta+)}/P_L$	$P_{(\delta-)}/P_L$	% difference P_V	% difference P_δ	σ_x/F_{xc}
1 (A)	0.824	1.031	1.020	1.048	1.044	−1.1%	1.5%	0.327
2 (A)	0.868	1.042	1.048	1.040	1.040	0.6%	−0.2%	0.330
3 (A)	0.868	0.754	0.768	0.757	0.766	1.5%	0.8%	0.239
4 (A)	0.868	0.842	0.879	0.871	0.871	3.8%	2.9%	0.267
5 (A)	0.957	0.880	0.949	0.885	0.879	7.0%	0.3%	0.279
6 (A)	0.959	0.814	1.344	0.832	0.824	53.0%	1.4%	0.258
7 (A)	0.960	0.906	1.074	0.907	0.907	16.8%	0.1%	0.287
8 (A)	0.991	0.882	1.078	0.888	0.882	19.6%	0.3%	0.279
9 (A)	1.002	0.798	1.048	0.799	0.796	25.0%	0.0%	0.253
10 (A)	1.013	0.749	1.036	0.740	0.744	28.6%	−0.7%	0.237
11 (B)	0.597	0.973	–	0.983	0.983	–	1.0%	0.680
12 (B)	0.597	0.898	–	0.918	0.918	–	2.2%	0.627

laboratory's interior lights were extinguished in order to lessen the effects of ambient light on the moiré picture. The light source was switched on in order to begin observing the initial moiré fringe pattern.

The test was run at a stroke rate of at 2.5 mm/min, which was slow enough to observe the growth of the fringe pattern, yet provided reasonable test duration for taping purposes. Once a loading of approximately 4.5 kN was achieved, the test was held at that load as efforts were made to zero the initial fringe pattern and attach the lateral LVDT used to measure lateral displacements. Once a satisfactory initial fringe pattern was achieved, the test resumed and continued until ultimate column failure. After failure, the actuator was returned to its initial position and the frame was prepared for the next experiment. The following observations were made.

First, all columns had surface imperfections that caused initial fringes to appear. When processing the data, these initial fringes are subtracted from the overall fringe orders obtained throughout the duration of the test. Next, the compression-side of the column had more fringe patterns than the tension-side as buckling developed in the intermediate length columns. Along with the increased number of fringe patterns, a lower wavelength was observed on the compression side (Figs. 5 and 6). Lastly, the final Euler displacement direction was dependent upon the mounting of the column into the shoes. If the web of the column were slightly to one side of the centerline of the pin, the column would have final lateral (Euler) movement in that direction. Physically this phenomenon makes sense and was accepted as an idiosyncrasy of the fixture because it does not prevent the Euler buckling mode from occurring. As the test progressed, no twisting of the column was observed.

The contour plot obtained by moiré (Figs. 5 and 6) measures out-of-plane deformations of the flange. Thus, it only provides the evolution of the local mode. The Euler mode causes deflections parallel to the plane of the flange. The Euler deformations cannot be seen on the fringe pattern. Therefore, an LVDT

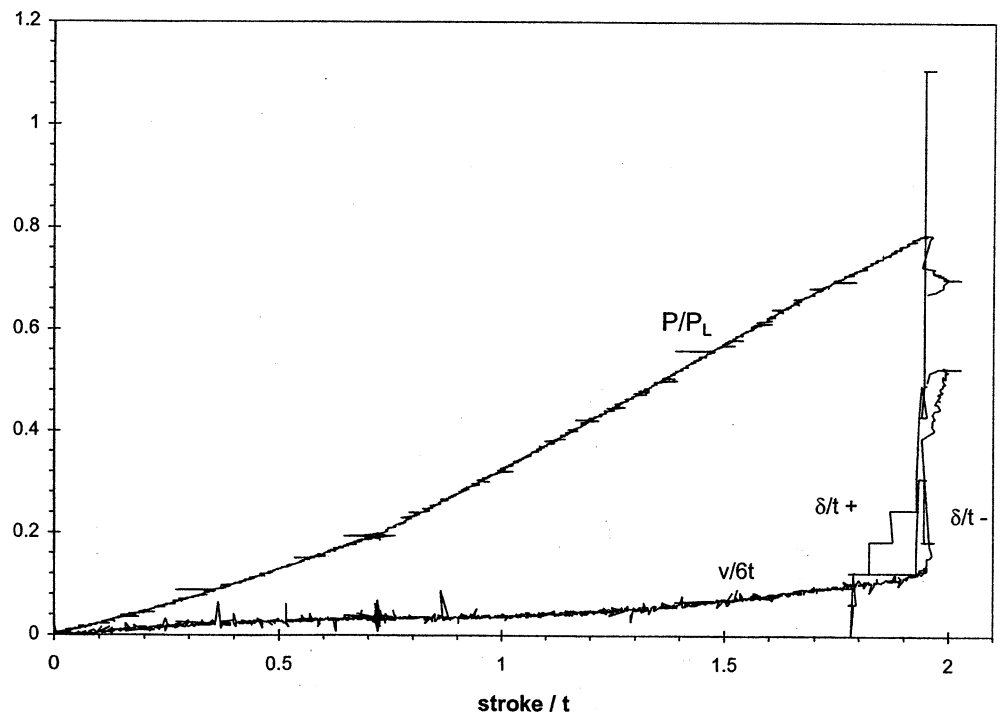

Fig. 7. Normalized load, lateral, and two flange displacements as function of stroke for sample 6.

was mounted to record the Euler mode (Fig. 4). The contour plot is useful only to see the local mode. To see the interaction among the local and Euler modes, one must look at Figs. 7 and 10 which depict all the information as continuous functions of stroke (proportional to time). Since the flange deflection δ can be measured everywhere on the flange, for all times, a decision has to be made of what numerical values to report. Here, the numerical values reported are the maximum deflections which occur at the tip of the flanges, at the midspan. This information was used to construct plots such as those shown in Figs. 7 and 10. Furthermore, the moiré data was used along with the Southwell method to compute the buckling loads $P_{\delta+}$ and $P_{\delta-}$ reported in Table 2.

4. Interpretation of experimental data

In this section, both the moiré and conventional data are combined in order to observe the buckling behavior of the column. The axial compression of the column, measured by the stroke LVDT occurs in the x-direction (u displacement, Fig. 1). Likewise, lateral deformations measured using the lateral LVDT act in the y-direction (v displacement). Measured parameters were normalized to combine all of them in one plot (Fig. 7). The load measurements P were divided by the appropriate isolated-mode buckling load P_I, whether it is local or Euler, depending upon the slenderness of the column. The Euler load P_E was computed with Eq. (1). The bending stiffness (EI) was back calculated (also w/Eq. 1) from the average of two long-column tests. The short-column buckling load P_L was obtained as the average of two short-column tests. Both (EI) and P_L are considered to be section properties independent of the length. These values are routinely reported by the manufacturers of pultruded structural shapes (Table 1).

After a test was completed, the VCR tape was played to capture the number of fringes as function of the load. The number of fringes was converted into flange displacements δ, which are normal to the flange surface. Because of the non-symmetrical nature of the flange displacements δ it was necessary to count the fringe order on both sides of the flange. The two sides are designated by "+" or "−", which represent fringes on the more compressive or less compressive side respectively. The more compressive side is defined as the side with higher compression stress due to the contribution of the Euler mode. In the case of a pure local buckling mode, the two flange (δ^+,δ^-) displacement measurements are equal. The non-dimensional out-of-plane displacements (δ^+/t, δ^-/t, where t is the flange thickness reported in Table 1 were combined on to the same plot with the non-dimensional transducer data (P/P_I and $v/6t$ vs u/t; Fig. 7) for each of the columns tested. From the plot of the combined non-dimensional data, it can be seen in a graphical manner which buckling mode occurs first. The presence of flange displacements (δ^+/t, δ^-/t) indicates the presence of the local buckling mode, while lateral deformations ($v/6t$) indicate the presence of the Euler buckling mode. The apparent stepping of the data is caused by the discrete nature of the measurement technique, which consists of counting a discrete number of fringes.

Previous research (Barbero and Tomblin, 1994; Tomblin and Barbero, 1994; Barbero and Trovillion, 1998) showed that Southwell's data reduction technique could be used to determine the isolated-mode buckling load for an imperfect column. The technique, reported extensively by Tomblin and Barbero (1994) is based on the assumption that the plot of P–δ acts as a rectangular hyperbola, with the load-axis and the horizontal line $P=P_C$ as asymptotes, with P the measured load, and δ the measured deformation. If the horizontal asymptote can be determined, the critical buckling load would be known. It was shown that the slope of the best-fit line for the plot of δ/P vs δ is equivalent to the inverse of the critical buckling load $1/P_C$. Imperfections in the column effect the y-intercept of the plot, but not the slope. Therefore, the correct critical buckling load can be determined. In the past, this data reduction technique has been used for single mode buckling experiments (either global or local). As explained before, buckling-mode interaction is a combination of several modes. Therefore, it is possible to obtain

different estimates of the buckling loads for the same test, depending upon the data being used (stroke, lateral, or flange deformation.)

For each column tested the δ/P vs δ plots were made for both the LVDT (v) and moiré (δ) data. A linear regression was performed on the transformed data in order to obtain the equation for the best fit of the data. The results are presented in Table 2. The ultimate experimental load P_C, the critical buckling load determined from lateral LVDT measurements P_V, and the critical buckling load determined from the moiré measurements ($P_{\delta+}$, $P_{\delta-}$), were normalized by the isolated-local buckling load P_L. Next, the experimental results are described individually for two column lengths to illustrate the interactive buckling mode behavior.

4.1. Intermediate-length column

If buckling-mode interaction is not considered, a WF column of length $L = 2.18$ m (sample number 6) is expected to buckle at a critical buckling load of $P_I = 170$ kN which would correspond to a pure local mode. However, the observed buckling modes display noticeable contributions from both the local and Euler buckling modes simultaneously, thus providing tangible proof of buckling-mode interaction.

The ultimate experimental load $P_C = 138.1$ kN attained was 18.8% lower than the isolated-mode critical buckling load P_I. However, the buckling load is not the only determining factor, but rather the buckling behavior. From the moiré images and transducer data it can be determined that the column buckled with a combined mode. At $P = 138.1$ kN, the fully developed fringe pattern shown in Fig. 6 displays a 2:1 ratio in the number of fringe sets between the top half (δ^+) and the bottom half of the flange (δ^-), which in turn correlates to unequal wavelengths between the two halves. This is an indication that the two halves did not experience an equal amount of load (i.e., Euler contribution).

Fig. 7 was prepared to show the contributions of the buckling modes. The Euler mode is represented by the lateral deflection $v/6t$. The local mode is represented by the flange deflection δ/t. The column begins to experience small lateral deformation $v/6t$ almost at the onset of the test. The development of the lateral deformation is along a shallow path, yet is well developed when the first flange displacements appear. Once the flange begins to buckle, the lateral deformation increases at a higher rate. It can be seen that once the flanges begin to buckle, indicated by δ^+/t and δ^-/t, the local buckling mode develops more quickly than the Euler mode (indicated by the lateral deformation). The flange experiences out-of-plane displacements up to $\delta^+/t = 0.62$ and $\delta^-/t = 0.31$, before the column fails. Catastrophic failure occurs shortly after the appearance of the local mode.

Based on Southwell's technique applied to the lateral LVDT data the critical buckling load was calculated to be $P_V = 228.1$ kN, with an $R^2 = 0.94$, where R^2 is the regression coefficient (Montgomery and Runger, 1994). This value is 65.2% higher than the isolated mode buckling load P_I. The Southwell's load P_V is 50.2% higher than the ultimate experimental load P_C. Following an Euler mode only, the column should have failed at 228.1 kN, according to the lateral deformation data. Once the local buckling mode developed, the column experienced a coupling in the two modes, causing premature failure.

Similarly, the experimental load P was plotted as a function of the two measured flange displacements (δ^+, δ^-). The P–δ plot (Fig. 8) shows that the column displayed classical local buckling behavior of a weaker column. In other words, the load increases along a primary path ($\delta = 0$) with no deformation until its bifurcation point at a load of approximately 125 kN is obtained. Then the load continues to increase along a shallow path (secondary path) approaching 138.1 kN, while the flanges experience out-of-plane displacements approaching the thickness of the flange. Notice in Fig. 8 that the more compressive side δ^+ experiences approximately twice as much out-of-plane displacement as the less compressive side δ^-.

The Southwell plots (Fig. 9) for both moiré measurements were made to determine the critical

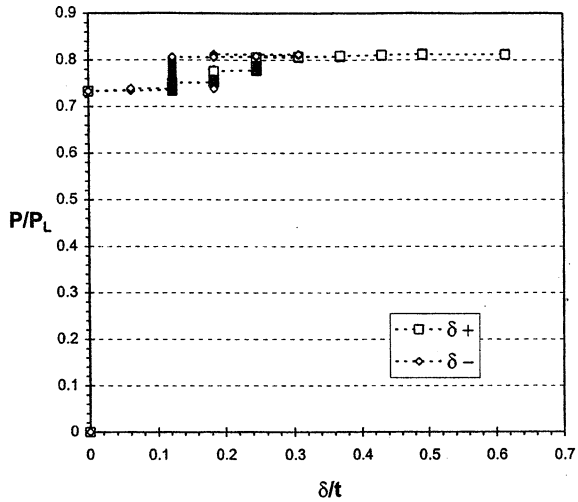

Fig. 8. Load vs flange deflection data for sample 6.

buckling loads. The linear best fit for the flange displacement data of the more compressive side δ^+ predicted a critical buckling load of $P_{\delta+}=141.2$ kN with an $R^2=0.999$. The best fit for the less compressive side δ^- predicted a critical buckling load of $P_{\delta-}=139.9$ kN, with an $R^2=0.994$. When compared to the isolated-mode buckling load, $P_{\delta+}$ and $P_{\delta-}$ were 16.9% and 17.7% lower than P_I respectively. The Southwell reduction for the moiré data provided an accurate prediction of the actual ultimate experimental load $P_C=138.1$ kN, with $P_{\delta+}$ and $P_{\delta-}$ giving percent differences of 2.3% and 1.3% respectively. The accuracy of the moiré Southwell data suggests that the tertiary mode has a strong component in the shape of the local mode. Therefore, the moiré data was not corrupted by the introduction of another buckling mode. Instead, the tertiary local buckling mode was the one being

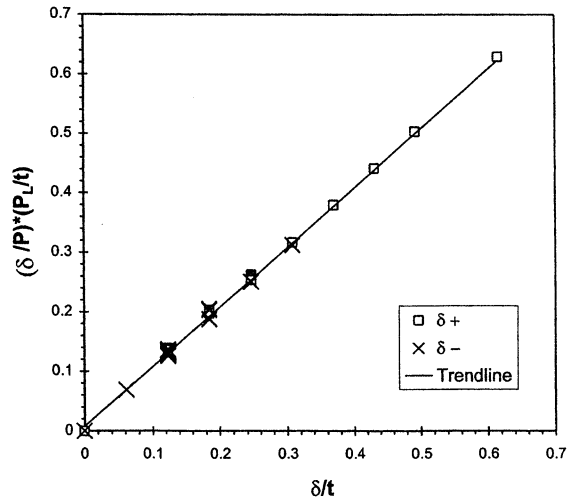

Fig. 9. Southwell plot of flange deflection for sample 6.

introduced into a system already being degraded by the Euler mode (indicated by the lateral deformation).

4.2. Critical-length column

If mode interaction is not considered, a WF column of length $L = 2.31$ m (sample number 10) would buckle at a load $P_I = 165.7$ kN, in a pure Euler mode. The experimental results presented in this section show that the 2.31 m long column failed due to buckling-mode interaction. The ultimate experimental load ($P_C = 127.2$ kN) attained was 23.2% lower than the predicted critical buckling load.

It can be seen in Fig. 10 that the column begins to experience lateral deformation $v/6t$ shortly after the onset of the test. The lateral deformation almost reaches its peak (not including lateral deformation after failure) before the flange displacements (δ^+, δ^-) appear. Therefore, it can be seen that the Euler mode develops first. The fringes on both the more compressed side δ^+ and the less compressed side δ^- appear simultaneously. Almost immediately after the flange displacements appear, the column fails. Once mode interaction occurs, the column fails catastrophically. This is an indication that the tertiary path (interacting path) is highly unstable.

The experimentally measured load P was plotted as a function of lateral deformation v/t in Fig. 11. It can be seen that the load does not follow a trivial primary path, but a lateral deflection (about 1.5 t) occurs before failure. This may occur due to initial imperfections in the beam or mounting eccentricity. The load increases to a peak of 127.2 kN, while simultaneously the lateral deformation increases at a relatively high rate. After the peak value is obtained, the load begins to decline and the lateral deformation continues to increase rapidly until ultimate column failure is obtained.

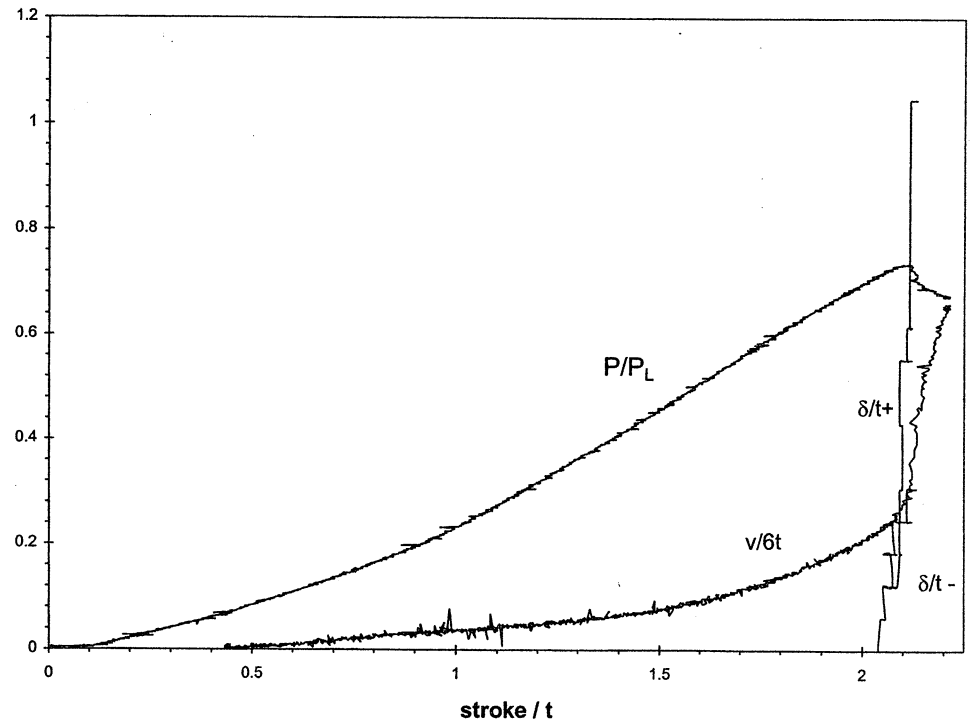

Fig. 10. Normalized load, lateral, and two flange displacements as function of stroke for sample 10.

Using the Southwell's technique, a linearized plot was made based on the data in Fig. 11. The best fit linear regression was performed in order to obtain the equation of the best fit line. The inverse of the slope, which corresponds to the critical buckling load, was calculated to be $P_V = 175.8$ kN, with an $R^2 = 0.996$. This value differs only 6.1% from the isolated-mode buckling load P_I. However, P_V was 38.2% higher than the ultimate experimental load $P_C = 127.2$ kN. The difference may be explained by the fact that the column was not weakened by the presence of the local bucking mode before lateral deformations were well developed. According to the lateral (Euler) deformation data the column should have reached 175.8 kN if it were not for the sudden appearance of the interacting mode at about 127.2 kN.

Similarly, the experimental load P was plotted as a function of the two measured flange displacements (δ^+, δ^-) and the same behavior depicted in Fig. 8 was observed. The column displayed classical local buckling behavior of a weaker column. In other words, the load increases along a primary path with no flange deformation until its bifurcation point at a load of approximately 127.2 kN. At this point, the load continues to increase along a shallow path (secondary path), approaching 133.5 kN while the flanges experience out-of-plane displacements up to $\delta^+/t = 1.04$ and $\delta^-/t = 0.32$, before column failure is obtained. Note that the ratio δ^+/δ^- of this column is higher than for sample 6 because of an increased influence of the Euler mode.

The linearized Southwell plot for both moiré measurements was made in order to determine the critical buckling loads. The linear best fit for the flange displacement data of the more compressive side (δ^+) predicted a critical buckling load of $P_{\delta+} = 125.7$ kN, with an $R^2 = 0.999$. The best fit for the less compressive side (δ^-) predicted a critical buckling load of $P_{\delta-} = 126.4$ kN, with an $R^2 = 0.999$. When compared to the isolated-mode buckling load, $P_{\delta+}$ and $P_{\delta-}$ were 24.2% and 23.7% percent lower than P_I respectively. The Southwell loads for the moiré data ($P_{\delta+}$, $P_{\delta-}$) provided an accurate prediction of the actual ultimate experimental load (P_C), with percent differences of 1.2% and 0.7% respectively. The accuracy of the moiré Southwell data is due to the fact that the flange displacements occurred after lateral displacements had appeared. Therefore, the moiré data was not corrupted by the introduction of another buckling mode. Instead, the tertiary mode is introduced into a system already being degraded by the Euler mode (indicated by the lateral deformation).

For this test it is clear that the Euler mode develops well before the local mode. The Euler mode

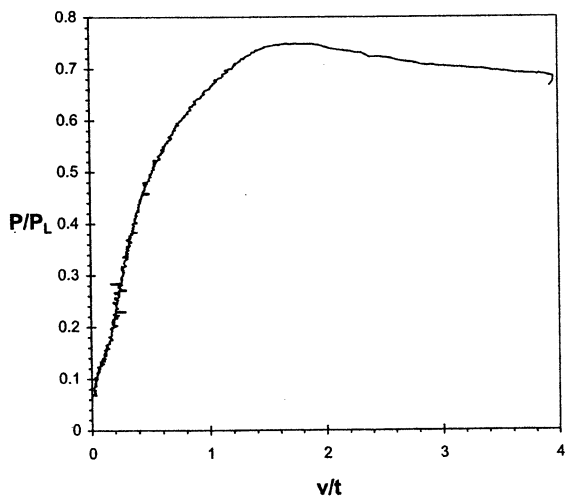

Fig. 11. Load vs lateral deflection of sample 10.

caused the flanges to buckle at 23.2% lower load than if the Euler mode was the sole cause of buckling. Therefore, from the presented data it can be determined that buckling-mode interaction occurs in the 2.31 m long column. The interaction between the two buckling modes (local and Euler) induced a tertiary buckling mode causing instantaneous catastrophic failure.

5. Discussion

When the columns are relatively short (e.g., $\lambda = 0.597$, samples 11–12), no significant lateral deflection is observed. Only the local mode develops, symmetrically with respect to the centerline of the flanges and no sudden failure occurs.

When $\lambda > 0.8$, the two isolated modes exist for all the columns as shown by the experimental local and Euler deflections observed. However, as long as the two isolated modes do not interact, the Southwell prediction based on either mode is good. Columns 1 and 2 are examples of this situation. Interaction did not take place until near the end of the test resulting in an ultimate load P_C close to the isolated mode load P_I. If the sample is virtually free of imperfections and the test rig is meticulously aligned, interaction will not lead to a reduction of failure load with respect to the isolated mode prediction. This has been shown previously in the shell experiments of Tennyson et al. (1971).

When the imperfections are large, the interactive mode develops earlier during the test. Then the column deforms in a single mode; in this case the interactive mode. Since the interactive mode contains flange and lateral components (δ and v), a Southwell analysis of any of them predicts the correct load. This is the case for column 3 and 4.

The results for columns 5–10 demonstrate that the Southwell prediction based on the Euler (lateral) deflection cannot predict the ultimate load, but it over predicts its value. Following the initial lateral load-deflection path it looks as if the column were to attain its isolated Euler mode load. But along the loading path, the interactive mode develops, cutting short the life of the column, as shown values $P_C < P_V$. Since the interacting mode has a strong component of the local mode, the Southwell analysis of the flange deformation data is able to correctly predict the ultimate load P_C. Note that the flange data predicts well P_C, not the isolated-local load P_L. This is because the isolated-local mode has been transformed completely into an interactive mode containing both flange and lateral deformations (δ and v).

The ratio of stress/strength (σ_x/F_{xc}) at failure is shown in Table 2. The experimental strength values F_{xc} for flange and web, given in Table 1, were measured from coupon tests (Barbero and Makkapati, 1988). The average stress through the thickness of the panels was computed using the modular ratio E_{web}/E_{flange}. The maximum value of the ratio stress/strength is reported in Table 2. Despite having the largest (σ_x/F_{xc}) values, samples 11–12 did not fail. On the contrary, they showed a flat, slightly stiffening postbuckling path, typical of isolated-local buckling behavior. On the other hand, samples 3–10 failed catastrophically in spite of having much lower stress. This further reinforces the conclusion that the failure of intermediate-length columns is due to unstable buckling behavior.

6. Conclusions

The most valuable tool used to display the buckling behavior of the various columns was the normalized plot of the measured parameters. Because the local and Euler buckling modes are characterized by two distinct measurable physical deformations (δ and v, respectively), it was possible to observe the contribution of each buckling mode to the interacting buckling mode. In this way buckling-mode interaction was shown for the pultruded WF-columns tested in this study. This interaction

between the modes is important because an unstable tertiary mode develops, leading to imperfection sensitivity and to a lower buckling load than predicted for either the local or Euler buckling modes acting alone. While the isolated local and Euler modes have stable post buckling paths, the interacting mode is unstable, as shown by the experimental data presented. From a design perspective, this may lead to a need for increased safety factors since unstable systems are highly sensitive to unknown imperfections.

Acknowledgements

This project was sponsored by the West Virginia Division of Highways under contract RP No. 131. The financial support is appreciated.

References

Arbocz, J., Potier-Ferry, M., Singer, J., Tvergaard, V., 1985. Buckling and Post-buckling. Springer-Verlag, Berlin.

Bank, L.C., 1989. Flexural and shear moduli of full-section fiber reinforced plastic (FRP) pultruded beams. Journal of Testing and Evaluation 17 (1), 40–45.

Banks, W.M., Rhodes, J. 1983. The instability of composite sections. In: 2nd Int. Conf. On Composite Structures, Paisley, UK, Elsevier, pp. 442–452.

Barbero, E.J., 1998a. Prediction of compression strength of unidirectional polymer matrix composites. J. Composite Materials 32 (5), 483–502.

Barbero, E.J., 1998b. Introduction to Composite Materials Design. Taylor & Francis, Philadelphia, PA.

Barbero, E.J., Makkapati, S., 1998. Compressive Strength of FRP Materials, Final Report SPN-T-699-FRP-1, West Virginia Division of Highways.

Barbero, E.J., Tomblin, J., 1994. A phenomenological design equation for FRP columns with interaction between local and global buckling. Thin-Walled Structures 18, 117–131.

Barbero, E., Trovillion, J., 1998. Prediction and measurement of the post-critical behavior of fiber-reinforced composite columns. Special issue on Civil Infrastructural Applications of Composite Materials 58 (8), 1335–1441.

Bazant, C.P., Cedolin, L., 1991. Stability of Structures. Oxford University Press, New York.

Brown, N.D., Mottram, J.T., Anderson, D., 1998. The behavior of columns for the design of pultruded frames: tests on isolated centrally loaded columns. In: 2nd Int. Conf. on Composites in Infrastructure, Tucson, AZ, vol. 2, pp. 248–260.

ByChrome 1995. Columbus, Ohio.

Esslinger, M., Geier, B., 1975. Postbuckling Behavior of Structures. CISM, Udine, Italy.

Foster, C.G., 1981. Interaction of buckling modes in thin-walled cylinders. Experimental Mechanics 21 (3), 124–128.

Galambos, T.V., 1988. Guide to Stability Design Criteria for Metal Structures, 4th ed. Wiley, New York App. B-4.

Gaylord, E.H., Gaylord, L.N., 1972. Design of Steel Structures, 2nd ed. McGraw Hill, New York.

Godoy, L.A., Barbero, E.J., Raftoyiannis, I., 1995. Interactive buckling analysis of fiber-reinforced thin-walled columns. J. Composite Materials 29 (5), 591–613.

Kabir, M.Z., Sherbourne, A.N., 1998. Lateral-torsional buckling of post-local buckled fibrous composite beams. ASCE J. Engng. Mechanics 124 (7), 754–764.

Kasagi, A., Sridharan, S., 1995. Modal interaction in composite cylinders under hydrostatic pressure. International Journal of Solids and Structures 32 (10), 1349–1369.

Montgomery, D.C., Runger, G.C., 1994. Applied Statistics and Probability for Engineers. Wiley, New York.

Optimas, 1993. BioScan Inc., Edmonds, WA.

PULTEX Design Guide 1999. Creative Pultrusions, Alum Bank, PA.

Schwarz, R.C., 1988 Determination of out-of-plane displacements and the initiation of buckling in composite structural elements, Experimental Techniques 23–28.

Strongwell, 1994. Strongwell Design Manual. Strongwell, Bristol, VA.

Tennyson, R.C., Muggeridge, D.B., Caswell, R.D., 1971. Buckling of cylindrical shells having axisymmetric imperfection distribution. AIAA Journal 9 (5), 924–930.

Tomblin, J., Barbero, E.J., 1994. Local buckling experiments on FRP columns. Thin-Walled Structures 18, 97–116.

Zureick, A., Scott, D., 1997. Short-term behavior and design of fiber reinforced polymeric slender members under axial compression. ASCE Journal of Composites for Construction 14, 140–149.